Journal of Manufacturing Processes 101 (2023) 1109–1123

Contents lists available at ScienceDirect

Journal of Manufacturing Processes

journal homepage: www.elsevier.com/locate/manpro

Stress characterization for friction-stir-welded electric vehicle battery trays with application of neutron diffraction

Nicholas Sabry [a,*], Joshua Stroh [a], Dimitry Sediako [a], Glenn Byczynski [b], Anthony Lombardi [b], Andrew Payzant [c]

[a] High-Performance Powertrain Materials Laboratory, University of British Columbia, 1137 Alumni Ave, Kelowna, BC V1V 1V7, Canada
[b] Nemak, Canada, 4600 G N Booth Dr, Windsor, ON N9C 4G8, Canada
[c] Oak Ridge National Laboratory, U.S. Department of Energy and Administered, 5200, 1 Bethel Valley Rd, Oak Ridge, TN, 37830, United States

ARTICLE INFO

Keywords:
Multi friction stir welded component
Residual stress
Straightening

ABSTRACT

The battery tray is an essential component that protects and controls battery-cell temperatures in electric and plug-in hybrid vehicles. The functional stress limit of the battery tray heavily depends on the residual stress acquired from the manufacturing process. Consequently, exceeding the stress limit of the battery tray during operation could compromise the battery-cell banks and may risk the vehicle's safety. Hence, understanding residual stress formation is vital for design and safety concerns. In the current study, AA 6061-plates were friction stir welded to an A365 high-pressure die-cast battery tray to create sealed coolant channels in the battery tray. However, this multi-material lap friction stir weld introduces residual stress into the battery tray, resulting in distortion. This distortion was mitigated using burnishing or coining operations, though straightening the battery tray had initially unknown effects on the residual stress. Therefore, neutron diffraction was utilized to characterize residual stresses after straightening. The results indicate that the friction stir welding (FSW) operation generated residual stresses exceeding the yield strength of the material, consequently deforming the battery tray by ±3 mm from the pre-weld geometry. The burnishing operation reduced the residual stresses below the material's yield strength while restoring the tray to within ±0.75 mm of the pre-weld geometry. Similarly, the coining operation restored the battery tray to within ±0.75 mm of the pre-weld geometry, however, increasing the number of locations where the residual stress exceeds the yield strength of the material.

1. Introduction

With the demand to produce economical, compact, and intricate products, there is a growing necessity for manufacturing operations that join components with significant differences in chemical composition that lead to notable differences in thermal conductivity, heat capacity, and coefficient of thermal expansion/contraction. Combining dissimilar material components allows for lighter and stronger designs at reduced costs. Traditional fusion welding of dissimilar materials is costly and time-consuming to such an extent that it is frequently unrealistic to accomplish for mass production [1]. This difficulty is primarily due to the differences in the joined materials' mechanical, physical, chemical, and metallurgical properties. Although there are difficulties to overcome, several researchers have demonstrated that the friction stir welding (FSW) method can successfully join similar and dissimilar materials [2–4]. Unlike fusion welding, FSW is a solid-state joining method that utilizes a non-consumable tool to join two materials below their melting temperatures. FSW joins materials via heat generated by a rotating tool that is plunged into the workpiece and then advanced along the weld joint, thereby mechanically mixing and forging plasticized material together [5]. The solid-state nature of FSW avoids bulk melting of the workpiece material, allowing the joining of dissimilar materials. While this method can effectively join dissimilar materials, the heat generated during the FSW operation leads to the evolution of residual stress [6–8]. One study, published by Richards et al., [9] describes how residual stresses in FSW arise from plastic misfit strains introduced due to the steep temperature gradients as heat is generated from the rotating tool and distributed into the component as the tool advances. Within the welding zone, the residual stress can form as both tensile and compressive, affecting the residual stresses in other areas of the

* Corresponding author.
E-mail addresses: nicholas@sabry-engineering.com (N. Sabry), joshua.stroh@ubc.ca (J. Stroh), Dimitry.Sediako@ubc.ca (D. Sediako), glenn.byczynski@nemak.com (G. Byczynski), Anthony.Lombardi@nemak.com (A. Lombardi), payzanta@ornl.gov (A. Payzant).

https://doi.org/10.1016/j.jmapro.2023.06.035
Received 28 March 2023; Received in revised form 2 June 2023; Accepted 12 June 2023
Available online 6 July 2023

component as they attempt to compensate, subsequently distorting the component. This distortion is usually not reported in single-welded studies as it is minimal; however, when considering components with multiple weld applications, it becomes significant. Usually, for single welded studies, maximum tensile residual stresses are on either side of the weld line, with lower residual stresses in between, forming an M-shaped residual stress profile distribution as described in [6–8]. However, the magnitude of stress and shape of the stress profile is influenced by the heat generation profile, which is asymmetric and is determined by tool geometry, rotational speed, traverse speed, and plunging force [10–13]. The asymmetric heat generation profile leads to non-uniform temperature gradients and, ultimately, thermal stresses. Masubuchi et al., [14] define thermal stresses as stress created by non-uniform temperature changes that, once equilibrated, generate residual stress. The non-uniform temperature change generated during FSW results in residual stress as the weld cools, generating compressive plastic strain as the material expands and contracts due to the heat generated at the source [6]. Feng et al., [15] explain that the plastic strains that accumulate during the thermal weld cycles are predominantly compressive and remain in the weldment. As the weldment cools to room temperature, tensile residual stresses of yielding magnitude are retained, typically leaving the base metal outside the weld region in a reduced magnitude compression. The internal tensile and compressive residual stresses deform the joint to comply with the strain compatibility. Therefore, the residual stress distributions and the resulting distortion depend on the final state of the plastic strain distributions. Leggatt et al., [16] state that tensile residual stresses are of yield magnitude (i.e., resulting in distorting the component) if the free thermal contraction of the heated material is restrained and that restrained contraction results in tension that exceeds the yield strength of the material. Additionally, Masubuchi et al., [14] list the risks of uncontrolled thermal stress, residual stress, and distortion: cracking and mismatching; high tensile residual stresses in areas near the weld causing fatigue damage, stress corrosion cracking and fracture under certain conditions; distortion and compressive residual stress in the base plate which can reduce the buckling strength of structural members. Therefore, the residual stresses and distortion in welded components must be controlled. Two methods for potentially controlling residual stress and its corresponding distortion are the burnishing and coining straightening techniques that are applied after the welding operation. Jayaraman et al., [17] describe burnishing as a low plasticity technique that introduces a surface layer of compressive residual stress that, when used post FSW, increases the high cycle fatigue endurance of the aluminum (Al) alloy by up to 80 % as compared to an un-burnished FSW weldment. On the other hand, the coining operation is relatively specific to individual component geometries. This operation requires specialized die tooling and a supportive structure below the component to deform the part to restore its geometry to the design specification. Hence, the coining operation is similar to the post-weld global mechanical tensioning (PWGMT) method described by Altenkirch et al., [18]. PWGMT is a stress levelling technique requiring high tensioning loads that exceed the cold weldment yield strength to elongate the weld material plastically, which deforms the component to restore its geometry to the design specification. The plastic deformation caused by the burnishing and coining of FSW components will uniquely impact the residual stresses in the component post-straightening. Consequently, analyzing the residual stress is crucial for optimizing the distortion and service life of any straightened FSW components. Fortunately, there are several methods to assess residual stress in FSW components. Woo et al., [19] used a direct in-situ neutron diffraction experiment to measure the temperature and thermal stresses in the FSW stir zone of the AA 6061-T6 alloy. Peel et al., [12] used X-ray diffraction to measure longitudinal and transverse stresses between similar-alloy aluminum FSW. He et al., [11] used a common but less reliable stress measurement technique (i.e., hole-drilling) on similar-alloy aluminum FSW in a butt joint configuration. The use of either a butt or lap weld configuration primarily depends on the design of the component. Nevertheless, Kumar et al., [20] found that, where possible, the use of a lap weld is preferable as the joined materials produce improved joint strength compared to a butt configuration weld. However, the studies [11,12,19] mentioned above focused on butt joint welding of similar aluminum alloys with no connection to tangible component distortion. There have been few attempts to understand the residual stress in a lap weld configuration with dissimilar aluminum alloys and even fewer on how straightening operations affect the residual stress in a multi friction stir welded component. Therefore, this study plans to understand different stress states formed during these processes. This insight into stress redistribution and relief during each process enables automotive manufacturers to minimize residual stress generation. Therefore, these results are critical for process optimization to minimize tensile stresses. The residual stresses were determined by employing neutron diffraction to perform several line scans along and through the FSW lap joints in the battery tray before and after applying two different straightening operations (i.e., burnishing and coining).

2. Experimental details

2.1. Materials and weld process

The battery tray examined in this study was produced at the Nemak Alabama facility in Sylacauga, AL, USA. Production of the battery tray also involved joining several 6061-T6 aluminum plates to a high-pressure die-cast (HPDC) A365 aluminum battery tray using FSW with varying thicknesses in a lap weld configuration. Fig. 1 (a) shows a rendering of the cast aluminum battery tray and the 6061 aluminum sheets, while Fig. 1 (b) shows a magnified section view of the weld region along with the FSW tool geometry, tool rotation direction and weld path.

The HPDC process is limited in creating internal geometries; therefore, requiring FSW to seal all exposed cooling channels with 6061 plates (see Fig. 1a). The FSW tool consists of a 12 mm diameter shoulder that is filleted to a 14 mm diameter with a triangular M12 threaded pin at a 2.2 mm length (see Fig. 2b). Welding is divided between peripheral and non-peripheral welds (see Fig. 2), with different traverse speeds, rotational speeds, and plunging forces shown in Table 1. Please note that an NDA protects the values in Table 1; regardless, the magnitude values are irrelevant to this study's purpose. Instead, the relative magnitudes are the critical consideration when comparing each weld group and are provided in reference to each welding group. For example, the traverse speed (C), rotational speed (D), and plunge force (E) utilized for the non-peripheral welds is double compared to the peripheral welds (see Table 1).

The 6061 (wrought) and A365 (cast) alloys are dissimilar for several reasons. A few of these reasons include the difference in post-processing of wrought alloys compared to cast alloys, resulting in a distinction between precipitates or grains that locally change the stiffness and other properties. Secondly, the compositional difference between A365 and 6061 alloys creates critical phases for strength or other properties specific to the alloy and its processing. One such property vital for casting the A365 alloy is fluidity when the molten material is injected into the die during the HPDC operation [21]. Fluidity increases with additional silicon, and for this reason, there is a significant difference in silicon between A365 and 6061, as can be seen in Table 2.

Additionally, differences in thermal expansion coefficients between the two alloys (A365 at ~21 μm/m-K and 6061 at ~24 μm/m-K) could have implications as the materials are heated and cooled through welding [22].

2.2. Post weld straightening

The utilization of multiple friction stir welds in the manufacturing process of the battery tray results in significant distortion of the primary geometry of the structure (Fig. 4). As a result, the battery tray requires

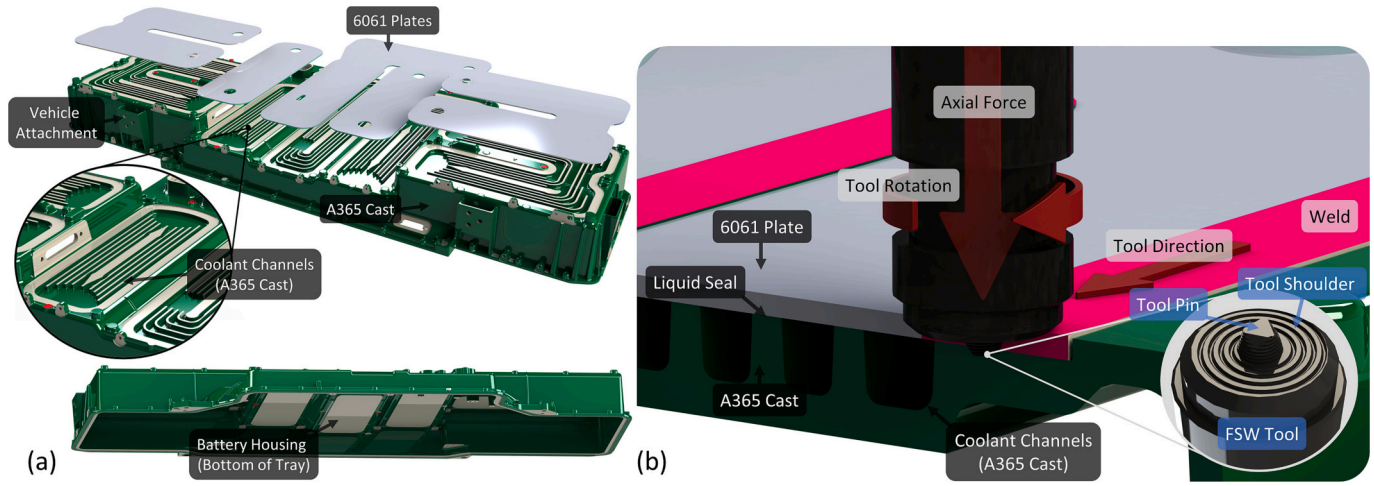

Fig. 1. (a) Battery tray coolant channels/cast structure and plate position (b) Cross-section of battery tray coolant channel with weld path in magenta. (For interpretation of the references to colour in this figure legend, the reader is referred to the web version of this article.)

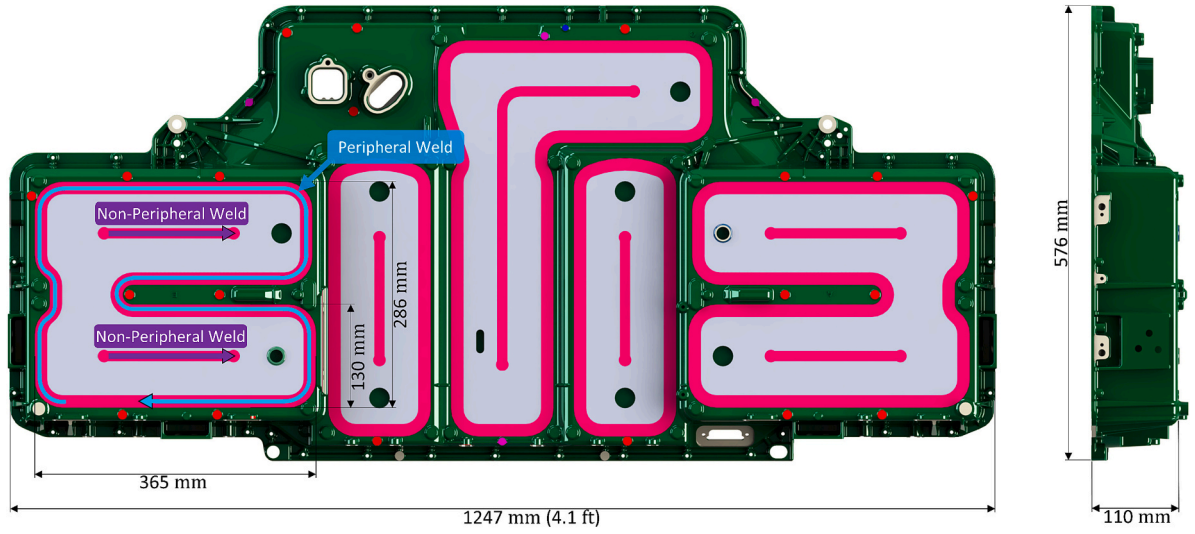

Fig. 2. Peripheral (blue) and non-peripheral (black) weld placement on the battery tray. (For interpretation of the references to colour in this figure legend, the reader is referred to the web version of this article.)

Table 1
FSW processing conditions.

Weld type (order welded)	Plunge depth (mm)	Dwell time (s)	Traverse speed (mm/min)	Rotational speed (RPM)	Plunge force (kN)	Plunge feed (mm/min)	Withdraw feed (mm/min)
Non-peripheral (1st)	A	B	C*2	D*2	E*2	F	G
Peripheral (2nd)	A	B*6	C	D	E	F	G

Table 2
6061 and A365 chemical composition (shown in wt%).

	Si	Mg	Cu	Fe	Zn	Mn	Cr	Ti	Ni	Sr	Al
6061	0.70	0.90	0.30	0.60	0.20	0.05	0.3	0.10	0.05	**	Bal.
A365	9.73	0.17	0.004	0.11	**	0.560	**	0.07	**	0.02	Bal.

post-weld straightening. The current study examined the residual stress distribution for the burnishing and coining straightening techniques as an effective way of reducing distortion (Fig. 3).

In Fig. 4, the CMM image shows that the most significant distortion is in the Z direction for the non-straightened tray. More specifically, the center portion of the non-straightened tray experiences between −1.5 to −3 mm of distortion, while the left and right wings experience a + 3 mm distortion. Following the burnishing or coining operation, the battery tray geometry was restored to ±0.75 mm of the pre-weld geometry.

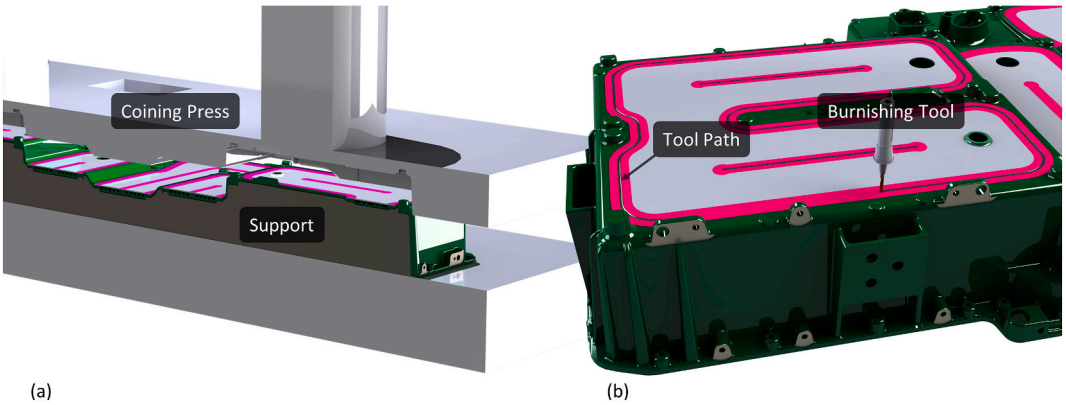

Fig. 3. (a) Cross-sectional view of the coining operation straightening via a hydraulic press supported on the inverted side (b) Burnishing tool straightening via surface layer compression.

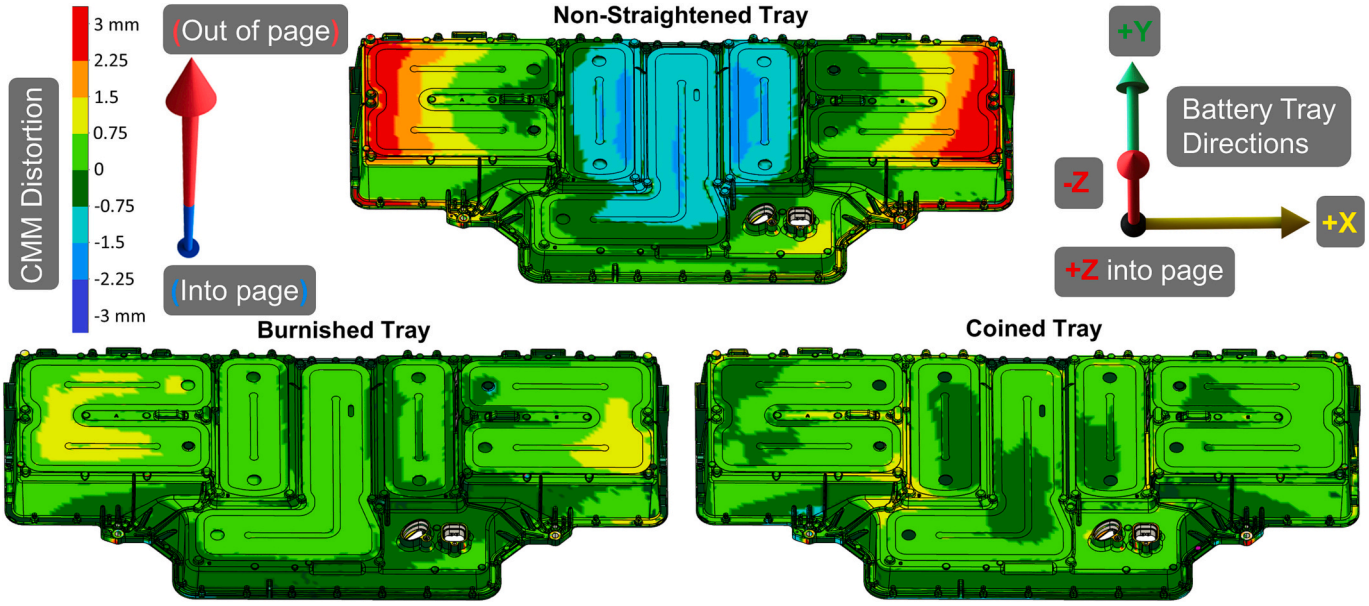

Fig. 4. Coordinate machine measurement (CMM) for the non-straightened, burnished, and coined tray (out-of-page distortion shown in red and into-page distortion shown in blue). (For interpretation of the references to colour in this figure legend, the reader is referred to the web version of this article.)

2.3. Neutron diffraction

Neutron diffraction experiments were conducted in the High Flux Isotope Reactor facility at the Oak Ridge National Laboratory (ORNL) in Oak Ridge, TN, USA, on the HB-2B High-Intensity Diffractometer for Residual stress Analysis (HIDRA) instrument. The neutron beam measured three orientations of strain (longitudinal-X, transverse-Y, and normal-Z) on the battery tray. The strain and, ultimately, the stress were calculated using the peak-shift method of diffraction patterns obtained from the {311} crystallographic planes of the aluminum lattice [23]. The peak-shift method requires a stress-free diffraction pattern from a material with the same composition, microstructure, and processing history as the component of interest. Therefore, a comb-style set of stress-free samples were extracted from identical battery trays, similar to the methods used in [23,24]. The length of each stress-free "matchstick was 20 mm and had a cross-sectional area of 3×3 mm^2. A gauge volume of $2 \times 2 \times 10$ mm^3 was used for the stress-free interplanar spacing, d_0, and the battery tray's stressed interplanar spacing, d, measurements. The scanning region (see Fig. 2) was confined to the leftwing of the battery tray due to the limitations of the HIDRA instrument (i.e., restricted to a working area of ~400×400 mm^2) and consisted of five scan lines: the −81 mm line (blue), 0 mm line (red), +81 mm line (yellow), extended 0 mm line (orange), and the cast line (purple), as shown in Fig. 5. Each dotted grey line in Fig. 5 corresponds to a weld line on the battery tray at 0, 56, 112, 155.5, and 213 mm with respect to instrument zero. Fig. 5 also depicts a slice removed from the tray strictly to visualize the cast line's internal points. The red, blue, yellow, and orange scan lines took place 2 mm deep into the 6061-plate, while the purple scan line took measurements inside the A365 cast material at varying depths up to 10 mm from the surface. Each scan line was measured on the non-straightened, burnished, and coined battery tray. Following scanning for all battery trays, residual strain, ε, was calculated utilizing Eq. (1) for three orientations (longitudinal-X, transverse-Y, and normal-Z).

$$\varepsilon_{xyz} = \frac{d - d_0}{d_0} \tag{1}$$

Where d_0 is the stress-free d-spacing, and d is the measured d-spacing from the diffracted Al {311} planes in the gauge volume. Following strain calculations, stress can be determined by employing Hooke's Law (Eq. (2)) for all three orientations due to the elastic nature of residual stress [23].

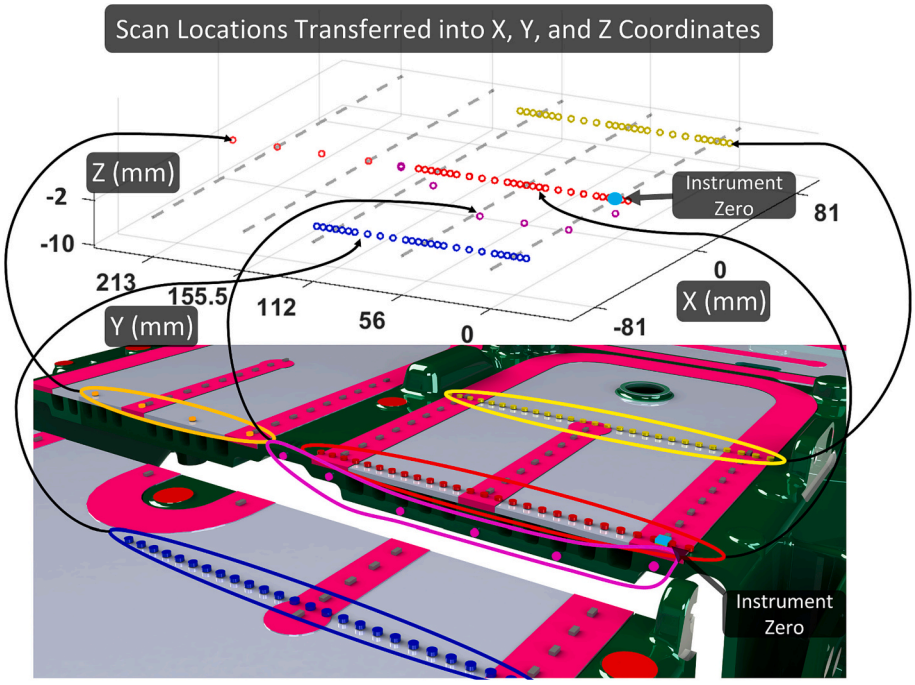

Fig. 5. Scanning region for the battery tray on HIDRA instrument.

$$\sigma_{x,y,z} = \frac{E_{hkl}}{1+\upsilon_{hkl}}\left[\varepsilon_{x,y,z} + \frac{\upsilon_{hkl}}{1-2\upsilon_{hkl}}\left(\varepsilon_x+\varepsilon_y+\varepsilon_z\right)\right] \quad (2)$$

where σ is the stress in MPa, E is the modulus of elasticity in GPa, and ν is Poisson's ratio. More details on the method and calculations can be found in Sabry et al., [25]. For residual stress calculations, the battery tray is divided into three distinct materials: cast (A365), FSW (6061 material directly on the weld), and base (6061 material not welded). The corresponding modulus of elasticity and Poisson's ratio, required for stress calculations, are obtained from tensile tests (see Fig. 6b).

2.4. Tensile sample preparation

Uniaxial tensile testing was conducted on several tensile samples cut out of multiple parts of the battery tray; A365 cast, base 6061 (unwelded region), cross 6061 (samples across the weld), and direct 6061(samples directly from the welded region) (see Fig. 6b). The 6061 samples were cut out of all three trays (i.e., non-straightened, burnished, and coined) to check for variability in results due to straightening. Each sample was machined following the principles outlined in the ASTM Standard E8/E8M-16a [26]. Strain measurements were obtained using an extensometer, maintaining a constant strain rate of 0.5 mm/mm/min throughout the tensile testing. Following the tensile tests, the ultimate tensile strength (UTS), yield strength (YS) at 0.2 % strain, young's modulus, and elongation were determined from the measured tensile data.

3. Results and discussion

3.1. Tensile testing

The tensile test results show that the FSW operation influences some of the mechanical properties of the 6061 material once welded. For example, the cross-weld samples fractured right above the weld during testing; therefore, the tensile properties of these tests are of the weld-affected regions and not the weld itself, as shown by the fracture

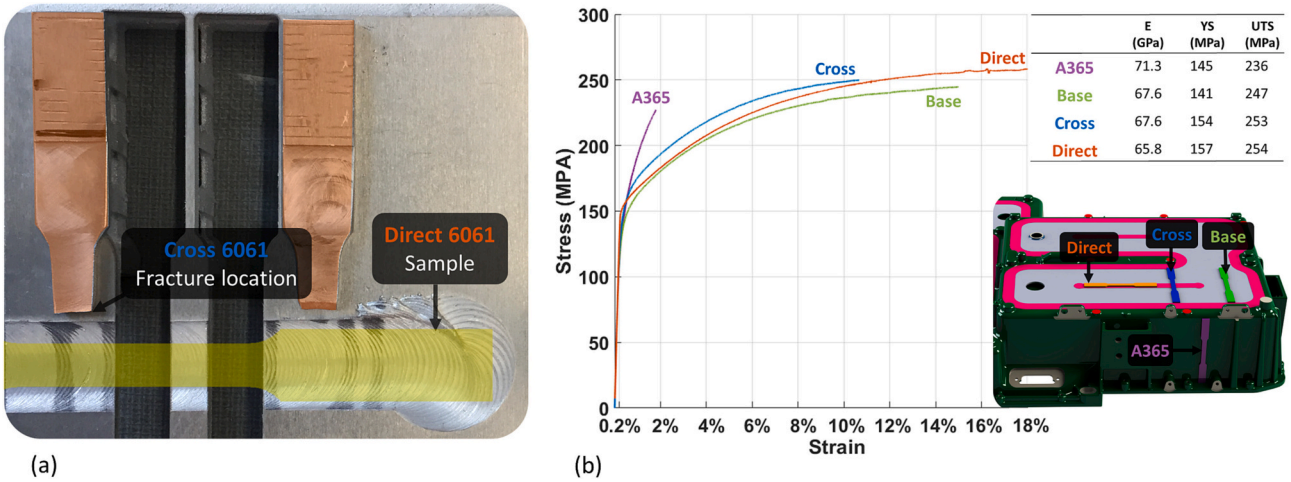

Fig. 6. (a) Fracture locations of cross-weld samples and direct-weld sample location (b) Tensile data of A365, 6061-Base, 6061-Cross, and 6061-Direct material.

locations in Fig. 6a. However, regardless of the fracture location, the modulus of elasticity (*E*) did not vary considerably between the base, cross, and direct weld-affected 6061 samples (see Fig. 6b).

The comparable modulus of elasticities between the base, cross, and direct 6061 material is attributed to the characteristics of the solid-state welding process. If the welding conducted primarily affects the microstructure and the material's elemental composition is retained, the modulus of elasticity tends to be insensitive to welding [27]. For the same reason, the samples taken from the burnished and coined trays had negligible differences in their modulus of elasticity. However, the yield strength seems to increase from the base 6061 (unaffected) to the cross 6061 (weld affected) and the direct 6061 (welded). This observation was consistent across the five samples tested for each condition, where the sample batch for a specific condition was within 5 % of each other's elastic modulus and yield strength values. The increasing yield strength from the base, cross and direct 6061 material is attributed to the worked, refined, and recrystallized microstructure due to the FSW process [28].

3.2. Residual stress in as-welded non-straightened tray

Fig. 7a indicates the location of three scan lines for each battery tray, as shown by the blue line at −81 mm, the red line at 0 mm, and the yellow line at 81 mm. The grey dotted lines correspond to the weld location on the model at 0, 56, and 112 mm from the component reference in Fig. 7a. The 3D stress profile is shown in Fig. 7b, and the corresponding projected 2D profile is shown in Fig. 7c. This data presentation method will be used throughout the remainder of this paper. Moreover, this paper will present data for the longitudinal-X, transverse-Y, and normal-Z directions (see Fig. 7a for directions), corresponding to residual stress measured in the X-direction, Y-direction, and *Z*-direction of each battery tray.

An evident change in the stress profile is seen going from the weld lines at 0, 56, and 112 mm to the base 6061 between them (see Fig. 7c) for the X-direction. Fig. 8, in addition to the X stress, displays stress in the Y and Z-direction, along with an enlarged image of the middle weld at 56 mm, which contains the plunging and traversing stages of the friction stir weld. Absent from Fig. 8's enlarged image is the "M" shaped residual stress profile that is characteristically found with the use of the standard flat shoulder and threaded circular pin FSW tools [6–8]. De Giorgi et al., [10] analyzed the effect of the shoulder geometry on the residual stress profile. As the tool geometry was modified, the tool's heat generation and its input to the material were influenced significantly. As a result, the tool geometry directly impacts the residual stress profile with such a magnitude that either tension or compression can be observed [10]. Therefore, with careful consideration of the tool geometry, the residual stress can be manipulated to obtain a desired profile and reduce component distortion post-welding.

The distinctions are apparent when comparing the tool geometry used to produce the battery tray (see Fig. 9) to the typical tool geometry that creates the "M" shaped residual stress profile seen in [6–8].

The enlarged view of Fig. 8 shows the stress profile across the friction stir weld. In this profile, there is an increase in residual stress at the center of the weld and lowering stress perpendicular to the weld on either edge, corresponding to the stress profiles and tool geometry seen in [1]. Additionally, the FSW operation also has changing magnitudes of residual stresses along the direction of the weld. Thus, while viewing the Y-direction of stress at the 56 mm weld in the enlarged image of Fig. 8, the stress is lower in the blue line (X-distance of −81 mm) than in the red (X-distance of 0 mm) and yellow line (X-distance of 81 mm). The difference in residual stress magnitude along the direction of the weld in the FSW process is likely due to the combination of the plastic deformation caused by the FSW tool's rotation and the material's cooling rate. When the FSW tool is first inserted into the material at the start of the welding process, it creates plastic deformation, which decreases residual stress in the transverse Y-direction. Then, as the FSW tool moves along the weld line, it continues to produce plastic deformation in the material, further reducing the residual stress in the transverse Y-direction. However, as the FSW tool reaches the end of the weld, the material in the transverse direction is more heated, softer, and more easily deformed than at the start, which causes the material to experience more deformation and produces more stress at the end of the weld. Therefore, as the material cools down, the microstructure changes and the material becomes stiffer; greater residual stress is then generated due to the associated high deformation at the end of the weld. This reasoning may be why the residual stress in the transverse Y-direction starts at a lower magnitude at the weld's start and then increases to a higher magnitude at the end of the weld. On the other hand, the longitudinal X-direction is less affected by plastic deformation compared to the Y-direction. This is because the tool is traversing in the X-direction and rotating the material into the Y-direction perpendicular to the traverse movement of the tool; therefore, the material in the Y-direction experiences much higher deformation compared to the X-direction. In comparison, the X-direction material is displaced parallel to the movement of the tool, causing much less deformation and generating less residual stress. The lower magnitude of stress in the *Z*-direction is due to significantly less contact area of the tool on the material in the Z-direction as only the tool side is in contact with the material. The larger difference in stress between the 56 mm weld and the 0, 112 mm weld is discussed in this publication [25]. This directionality in residual stress due to the weld tool's path could impact the profile of distortion throughout the tray. This suggests that the residual stress profiles and resulting distortion may be altered if the FSW tool path and direction are optimized.

In addition to the stresses measured on the weld lines as discussed above, the stress profiles developed in this study enabled analysis of

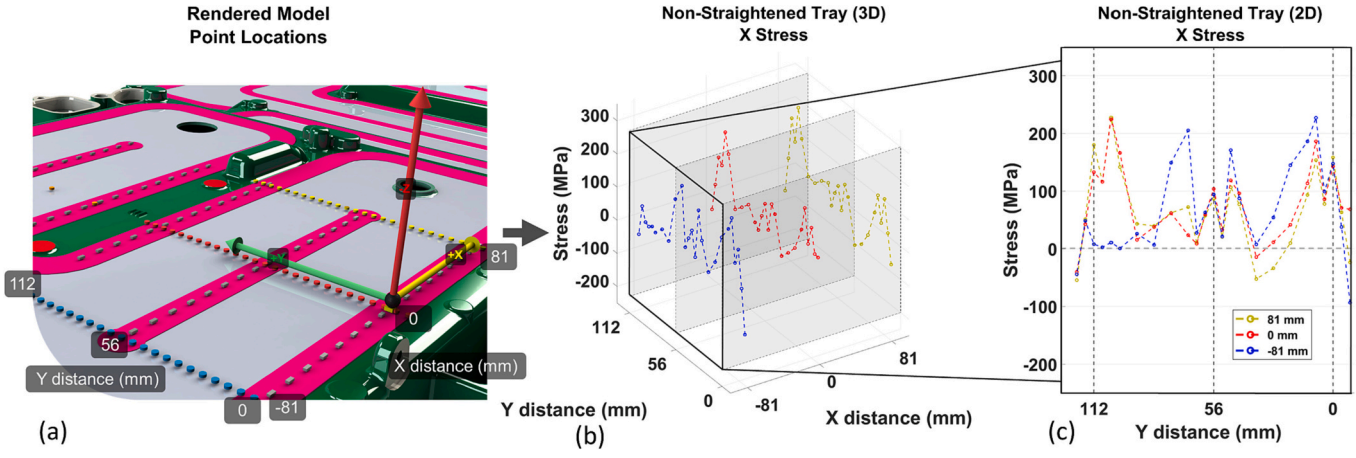

Fig. 7. (a) Visualization of scan point locations (b) Three-dimensional view of X-direction stress data (c) Two-dimensional view of X-direction stress data.

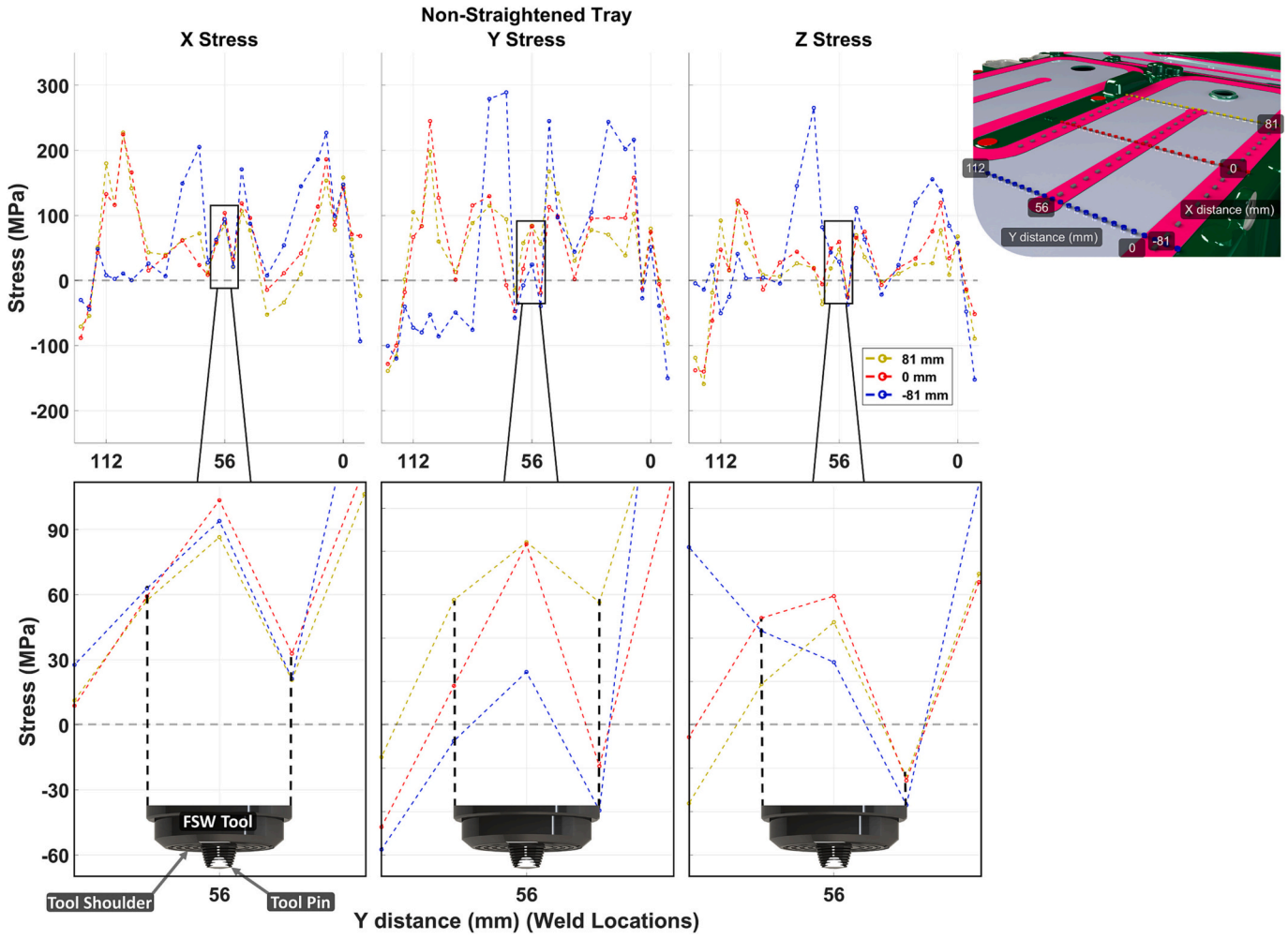

Fig. 8. X, Y, and Z stress directions (non-straightened tray).

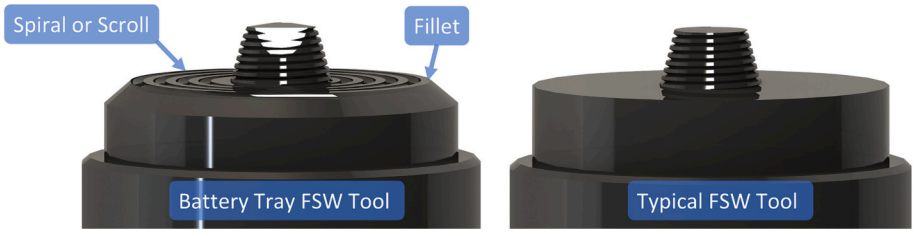

Fig. 9. Battery tray FSW tool compared to the typical FSW tool.

residual stresses with respect to the component and FSW geometry (see Fig. 10). The results of the stress profiles in Fig. 10 illustrate that the yellow and red scan lines go into tension (~200 MPa) on and near the weld lines. In contrast, the plate material between the weld lines becomes more compressed (~0 to −70 MPa). Each line shares this characteristic except for a portion of the blue scan line, as outlined in Fig. 10. Lower stress magnitudes characterize the blue line compared to the red and yellow scan lines around the 112 mm position, followed by a rapid increase in stress as the 56 mm weld position approaches. In addition, the stress profiles are comparable for all three lines in the regions encompassing the 56 mm and 0 mm positions. This is due to the blue line ending in an area with no welds at the 112 mm position, unlike the red and yellow lines. This weld positioning is different in the blue line compared to the red and yellow scan lines, as they have a weld at the 112 mm position, shown in Fig. 10b, leading to the maximum tensile stress at the outlined profile in Fig. 10a. This weld path design leads to considerable tensile stress in the valley between the 112 mm and 56 mm weld, possibly becoming the most strength-compromised region.

The neutron diffraction experiment included two more scan lines. The first is the extended orange line that advances into the adjacent 6061 plate, depicted on the rendered model in Fig. 11. The second line measured stress in the A365 cast material, shown by the purple dots on the green portion of the rendered model in Fig. 11. Fig. 11b-c translates the 3D view of the X-stress into the second dimension. In the foreground, the scan lines from the previous discussion are included (blue, yellow, and red plate scans) in high transparency to indicate the relative difference between the cast and plate scans without cluttering the image. The scan of the cast component had limited points; nevertheless, the purple A365-casting line follows a similar residual stress profile, in both shape and magnitude, as compared to the 6061-red line (see Fig. 11).

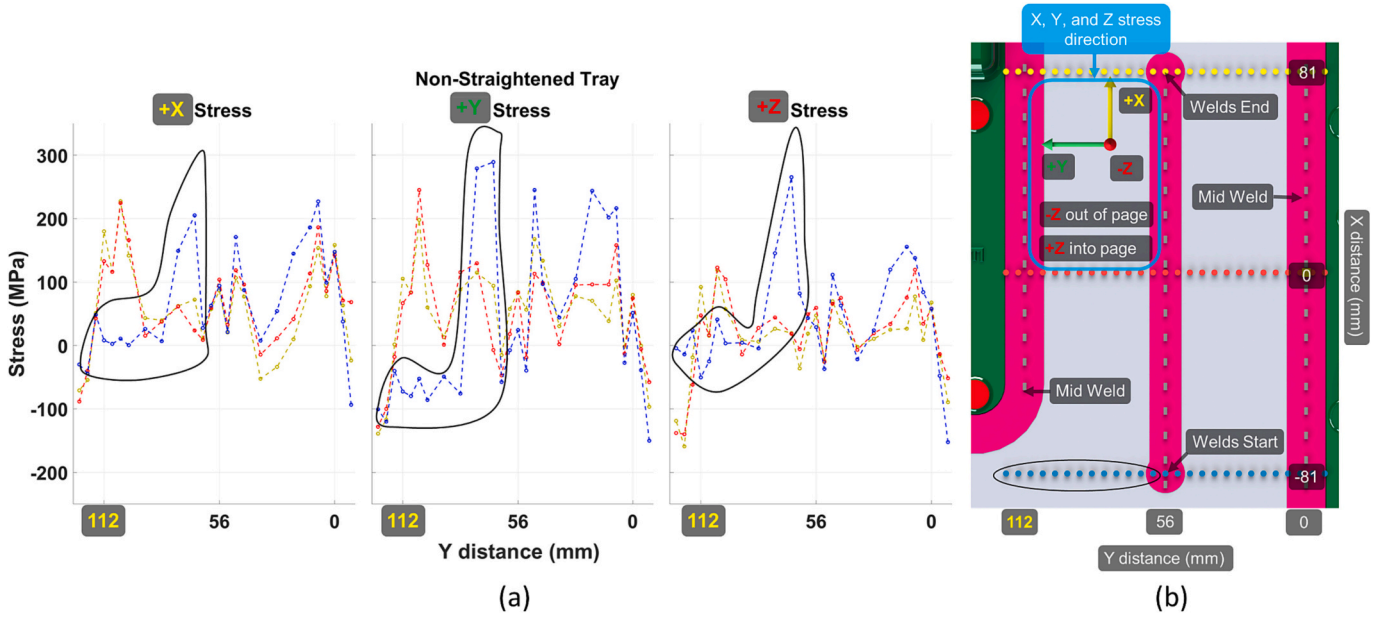

Fig. 10. (a) X, Y, and Z stress directions (non-straightened tray) (b) Top view of scanned location highlighting the start of the blue scanning line finishing absent of the weld. (For interpretation of the references to colour in this figure legend, the reader is referred to the web version of this article.)

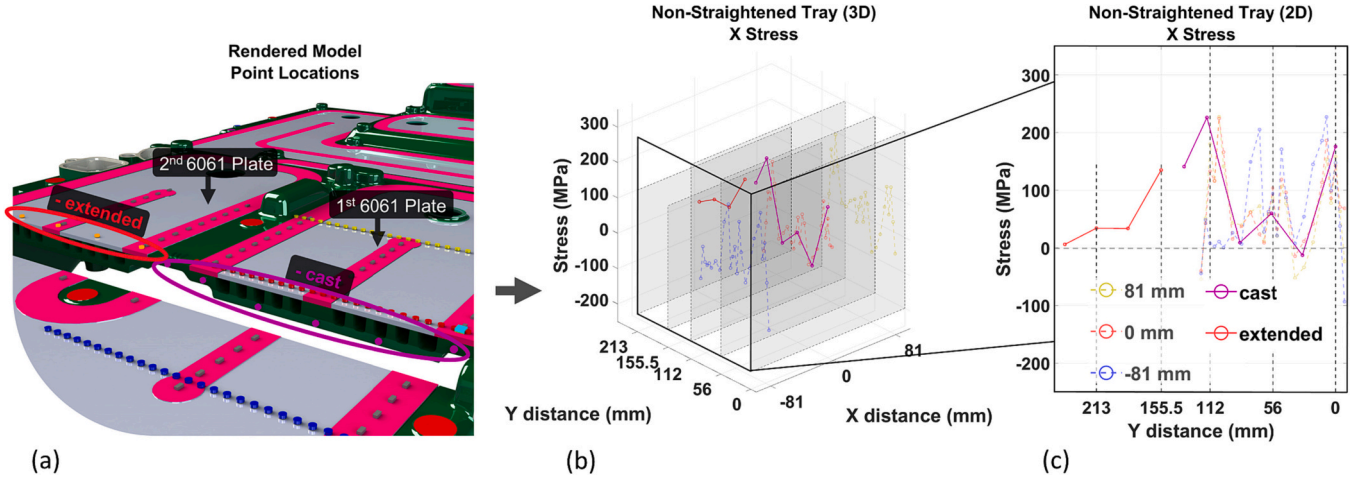

Fig. 11. (a) Visualization of scan point locations (b) Three-dimensional view of X-direction stress data (c) Two-dimensional view of X-direction stress data.

The Y- and *Z*-direction stress (see Fig. 12) follow the same pattern but are marginally higher in magnitudes between the welds.

The orange extended scan line measures residual stress in the second plate (see Fig. 12) on the 6061 material. This line is consistent with the red, blue, and yellow data measured in the first plate for the X direction, with high tensile stress on the welds and low to zero stress between the welds. However, this characteristic is the opposite in the Y and Z direction, with higher tensile stress between the welds and low to zero on the welds.

The stress difference between the first and second plates could be due to the sequence of operations. For example, the order, direction, and proximity of adjacent welds could impact the resulting residual stress profile. Many international standards give guidance on the proximity of fusion welds to avoid the possible compounding of residual stress between two joints to ensure that the combined stress during a components service does not exceed their allowable stress [29]. It is well known that there are various challenges with proximity fusion welding, from the development of harmful tensile residual stresses to the microstructural and strength changes in overlapping heat-affected zones as a result of multiple cycles of heating and cooling that occur due to welds in the proximity of other welds [30]. Concerning FSW, to the best of the authors' knowledge, specific standards for the proximity of solid-state welds and the residual stress measurements of solid-state welds in the proximity of another weld do not currently exist. Standards concerning the proximity of solid-state welds could be highly beneficial in maintaining the strength of components by avoiding the overlap of residual stress that could severely limit the service strength. The data presented in this study may be used to develop such standards for this phenomenon which is not well documented in the literature. FSW introduces heat into the material, which causes the 6061 plates to expand. However, the casting restrains the expansion of the 6061 plates on multiple sides, with the only free expansion side being upward. As the plate cools and contracts, it pulls on nearby "cold" material. The casting and the plate are experiencing similar thermal cycles, but the casting is likely receiving less heat due to the heat generation characteristics of FSW tools and the configuration of the FSW process [31,32]. This difference in heat input can result in a difference in the magnitude of residual stress between the casting and the plate. The casting will experience similar thermal

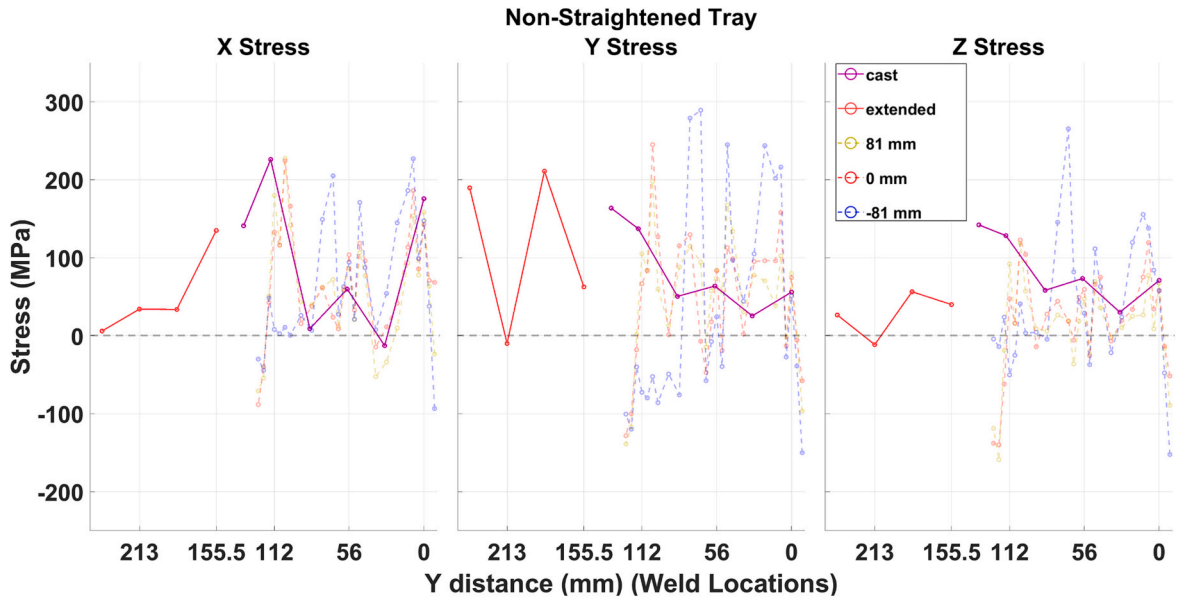

Fig. 12. X, Y, and Z direction of the cast and extended line scan.

contraction but with a reduced or modified magnitude of stress due to the variance in received heat and material restraint during thermal contraction. Additionally, since the plate is restrained in all directions (the direction of blue arrows in Fig. 13), the magnitude of stress seen in the plate will be higher than that seen in the casting (see Fig. 12).

3.3. Residual stress after burnishing and coining

The yield strength is a measure of the material's elastic limit, and once that limit is exceeded, the material will undergo plastic deformation. In comparison, residual stress is a measure of the stress that remains in the material after the material has experienced deformation, whether that deformation was elastic or plastic. Yet, in some cases, the residual stress can be higher than the yield strength and won't necessarily cause deformation as the residual stress is localized and locked inside the bulk of the material, which is restrained from all sides. Instead, it may indicate that the material has undergone significant plastic deformation, and the residual stress results from that deformation. It's important to note that residual stress is a measure of the internal stress in the material and not inherently the stress that caused the deformation. In other words, residual stress may be a result of deformation or a cause of deformation (distortion). In the case of distortion, areas of high residual stress may contribute to the distortion, but it is not innately a direct cause-and-effect relationship. Other factors such as material properties, geometric constraints, and loading conditions also play roles in determining the distortion. Residual stress is a complex

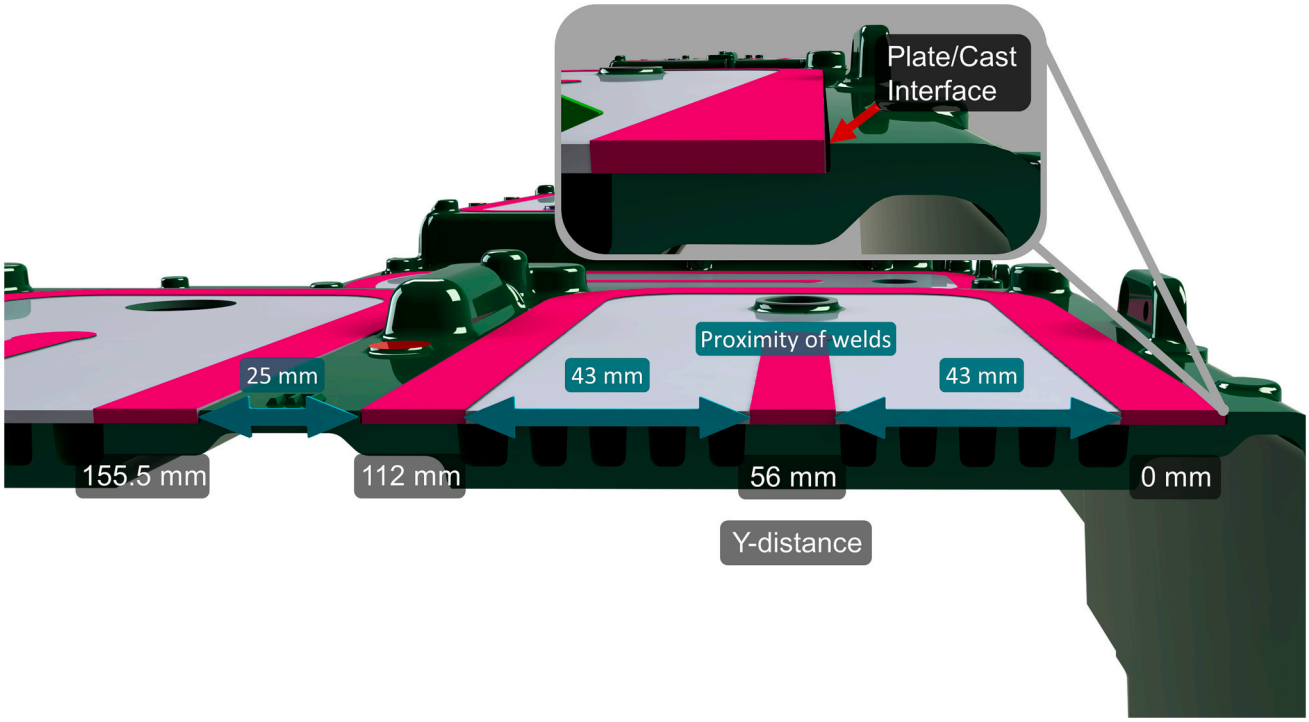

Fig. 13. Interface and the near proximity of welds between the 155.5 and 112 mm location.

phenomenon, and it is not only dependent on the yield stress but also other factors such as the thermal history, deformation history, and the mechanical properties of the material. Therefore, the following text will discuss the indications of connections between residual stress and distortion; however, a direct correlation between residual stress that is higher than yield strength resulting in plastic deformation and distortion may not be possible, but worth comparing nevertheless. For example, the non-straightened tray is extremely distorted (see Fig. 4), and the maximum tensile stress in the X-direction on the non-straightened tray is above the measured yield strength of the materials (see Fig. 6 for yield stress), possibly contributing to the distortion around the tray or indicating significant plastic deformation.

In comparison, many of the maximum stress measurements are at or below the material's yield strength after the straightening operations, as shown in Fig. 14. Fig. 15 projects the top of the surface of the 3D stress data into a 2D surface map. The 2D top view is shown in Fig. 15b, which displays the residual stress using a colour gradient between blue and red. For example, on the right side of Fig. 15b, a colour bar displays stress in MPa, where blue gradients indicate tension found directly on or near the welds. In contrast, the base metal between the welds includes yellow to red gradients, indicating less tension or, in some locations, compression. If the colour map contains hard-blue gradients (~200–300 MPa), then the residual stress is above the tensile yield strength of the 6061 material.

The heat maps shown in Fig. 16 compare the straightening effects on residual stress for the burnishing and coining operations. Considering "Area 1" on the blue scan line in Fig. 16, where this portion of the blue line is not on a weld line (see Fig. 10), the burnishing operation reduces this maximum tensile stress as compared to the non-straightened battery tray. On the other hand, the coining operation inverts the colour gradient, indicating that the tensile stresses have been converted into compressive residual stresses in most locations. In "Area 2," shown in Fig. 16, adjacent to the burnishing tool's indent path, the operation's effect on the stress map is seen in the red gradients, signifying substantial compressive stresses that seem to be beneficial in the reduction of distortion along the battery tray (see Fig. 4 for distortion map).

Additional data processing was completed to quantify the amount of residual stress above the material's yield strength, which is displayed in Fig. 17 as the yield area. The measured residual stresses within the yield area exceed the material's yield strength. The total yield area in the non-straightened tray is 24 % for the X-stress direction. The yield area is closely related to the position of the welds on the battery tray (Fig. 17). After the burnishing operation, the yield area reduces to 9.6 %. Similarly, the coining operation reduced the yield area to 9.8 % in the X-stress direction. The difference between the straightening operations is in the location where they reduce the yield areas. The burnishing operation reduces the yield area at each weld relatively evenly. In contrast, the coining operation is effective in regions at a distance from the casting edge, likely due to the edges in direct contact with the mounting table underneath the battery tray, as opposed to the middle of the tray, which is supported by a die and has some room to bend (see Fig. 3).

Next, considering the Y-direction of stress in the surface map shown in Fig. 18, the coining operation increased the yield area from 23 % to 46 %, covering a significant portion of the coined tray; this entire region is above the yield strength, suggesting that the operation exceeds the cold weldment yield strength, thereby plastically elongating the battery tray material resulting in residual stress. Furthermore, since the non-straightened tray is concave in geometry (see Fig. 19b) due to thermal contraction after welding, the coining operation is acting against the battery tray's concavity, where the black arrows in Fig. 19b show the direction applied force during the coining operation. Once the tray is pressed in the direction of the black arrows, the 6061 plates and upper part of the A365 are pulled and plastically deformed across the battery tray resulting in high tension (see Fig. 18, Coined Tray). The lower part of the component is not pulled but instead pushed, presumably resulting in compression, although this portion of the battery was not measured in this study. Despite the coining operation restoring the dimensional accuracy, this plastic deformation results in further tensile residual stress generation in the component. Although the distortion has been addressed, the higher tensile residual stresses may contribute to accelerated fatigue damage and stress corrosion cracking, possibly limiting the component's service life after the coining operation [33]. Conversely, the burnishing operation reduces the yield area considerably from 23 to 5.2 %. Specifically, near the top left corners of the surface maps, the non-straightened tray has a significant stress variance from compression to high tension exceeding the yield strength of the material near the 112 mm weld (see Fig. 18). The burnishing operation reduces the stress variance in this location to minimal compression or zero stress. In contrast, for the same location, the coining operation has

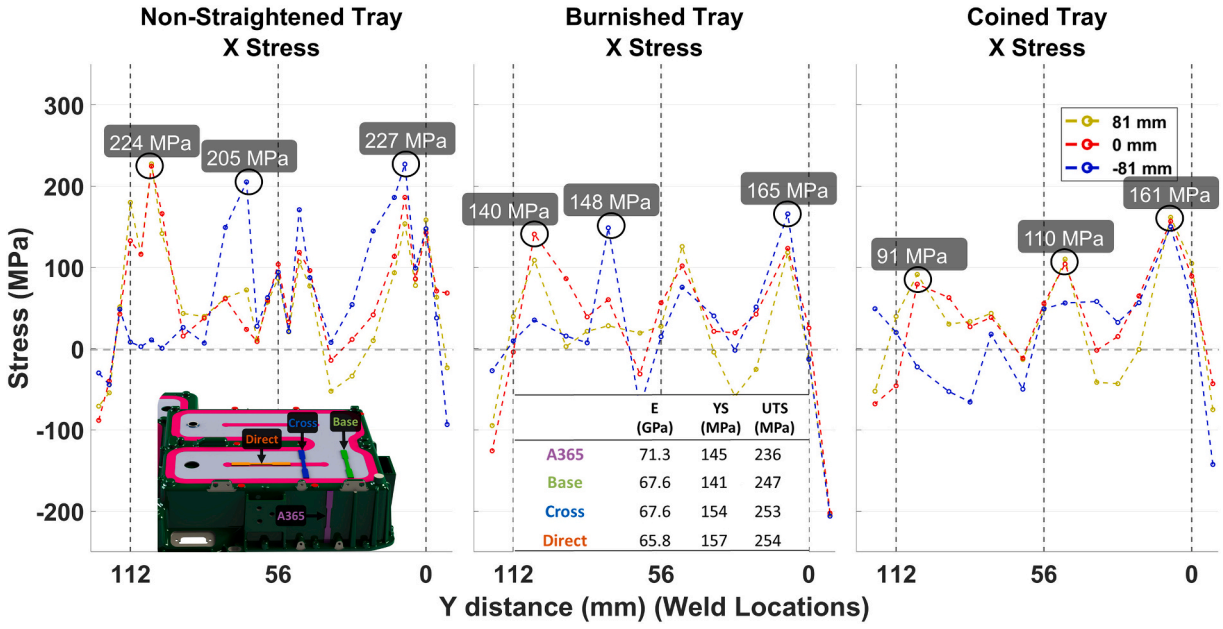

Fig. 14. Comparing stress measurements to yield strength after coining and burnishing.

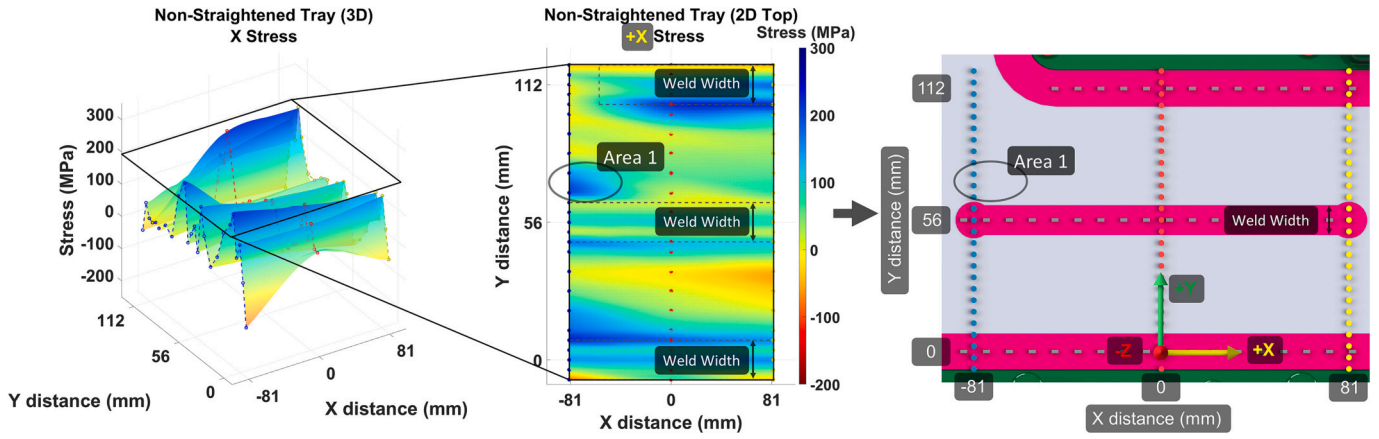

Fig. 15. (a) Three-dimensional view of X-direction surface data (b) Two-dimensional view of X-direction surface data (c) Visualization of scan point locations.

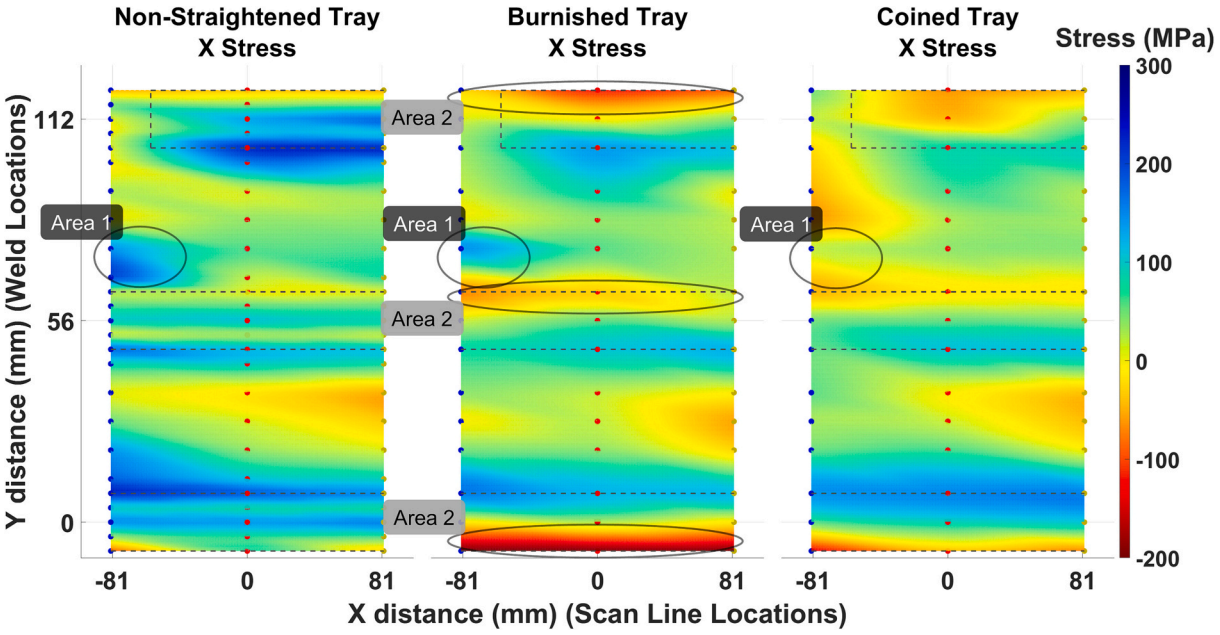

Fig. 16. Comparing (X-direction) non-straightened to burnished and coined stress map.

little effect and retains the high variance between significant compressive stresses to stresses exceeding the yield strength of the material, similar to the battery tray before straightening.

Considering the *Z*-direction of stresses in the surface map shown in Fig. 20, the coining operation slightly reduces the yield area from 6.1 % to 4 %, indicating constant low-level residual stress. On the other hand, the burnishing operation increased the yield area from 6.1 % to 16.3 %, suggesting that this process introduced more locations where the residual stresses exceeded the yield strength of the 6061 material.

The residual stress maps shown from Fig. 16 to Fig. 20 represent the stresses locked in the material's bulk. The observed stresses that exceed the yield strength and even ultimate tensile strength contribute to the initial deformation, following which the residual stresses remain in the component. Although not apparent in the short term, the remaining residual stress can contribute to long-term distortion and even possible cracking. However, the distortion developed over the long term (i.e., over a year) due to the release of residual stress is insignificant and should be on the magnitude of microns [34,35]. Although part of the residual stress is released into the initial plastic deformation, causing the concave curve of the battery tray (Fig. 4), the remaining residual stress is what can be measured in the non-straightened tray (Fig. 16 to Fig. 20).

The burnishing operation helped release the residual stress via plasticity along the weldments, leaving much-reduced residual stress in the X and Y directions while the non-critical *Z*-direction compensated. The residual stresses in the X and Y directions determine a significant amount of the distortion occurring in the battery tray, as these directions determine the concave geometry of the non-straightened battery tray. Therefore, the relatively higher residual stresses in the *Z*-direction won't affect the distortion considerably. In contrast, the coining operation strictly deforms the casting geometry adding to the residual stress.

Lastly, the effect of each straightening operation on the X-direction of residual stress in the A365 cast material is shown in Fig. 21. Comparing the stress profiles in the casting between all three trays reveals that the burnished tray experiences the lowest reacting tensile stresses, followed by the non-straightened tray. The coining operation introduces the highest magnitude of tensile stress in the casting. This is likely because the coining operation presses the entire tray, imparting significant force directly into the casting, translating into residual stress as it plastically deforms the tray into the product's specification.

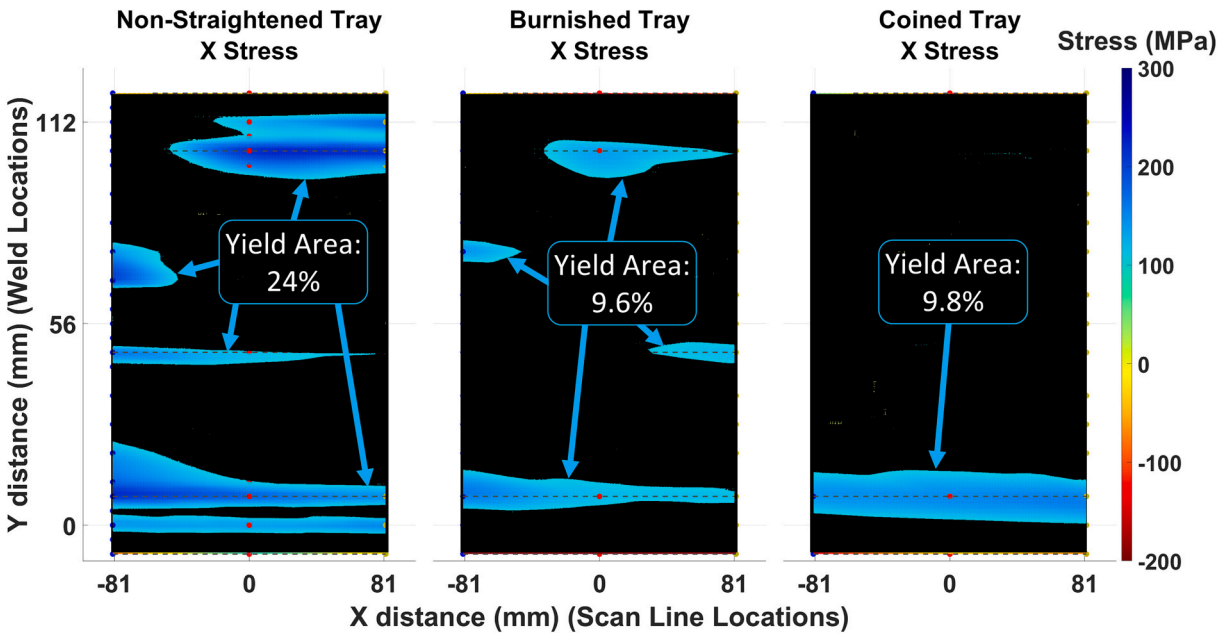

Fig. 17. Total yield area of the material is the addition of all the blue areas on the map. (For interpretation of the references to colour in this figure legend, the reader is referred to the web version of this article.)

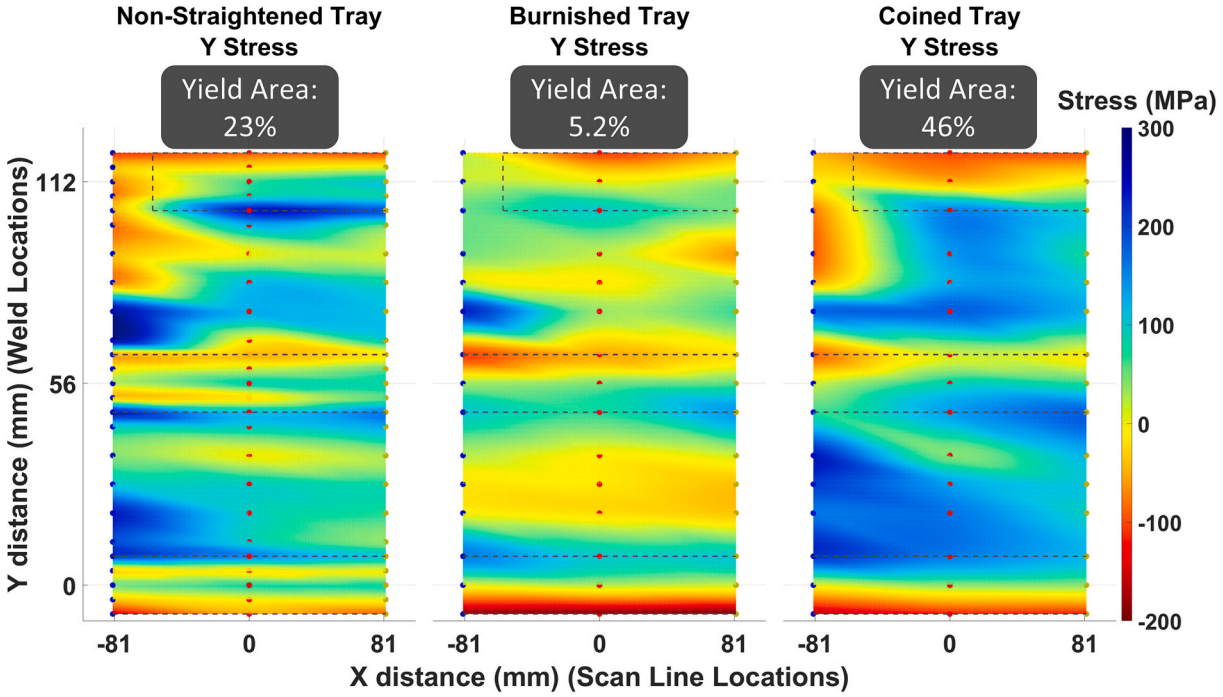

Fig. 18. Comparing (Y-direction) non-straightened to burnished and coined stress map.

4. Conclusions

This study uses a friction stir welding process to seal the coolant channels of an aluminum battery tray. Several 6061 plates were welded to an A356 HPDC structure in a lap weld configuration. Conducting multiple friction stir welds distorts the tray, requiring the implementation of a straightening process (i.e., burnishing or coining). The two straightening operations reversed the original distortion; however, the effect on the residual stress was unknown. Therefore, a comprehensive residual stress analysis was performed using neutron diffraction on the original distorted tray, the burnished tray, and the coined tray. The following conclusions may be drawn from this study:

(1) After the FSW process, the yield area (i.e., the area containing residual stress above the material's yield strength) accounted for 24, 9.6, and 9.8 % of the scanned area for the X-direction, Y-direction, and Z-direction of stresses, respectively.
(2) The FSW processes imparting significant plastic deformation led to large residual stresses shown in the yield area and the consequent distortion of the battery tray upwards of ±3 mm at the wings and center of the battery tray, as compared to the pre-weld geometry.

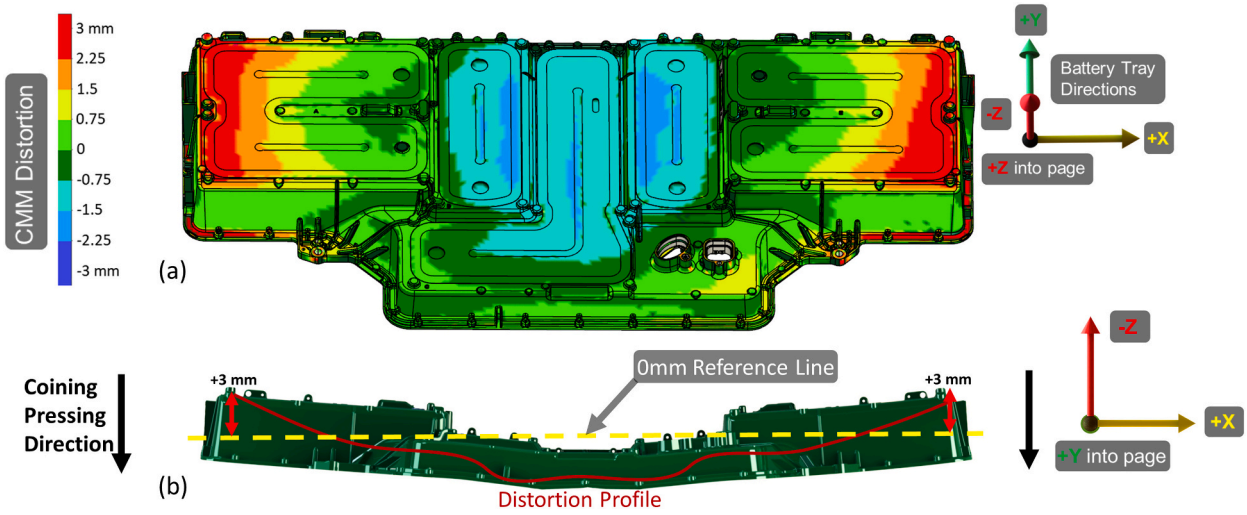

Fig. 19. (a) Non-straightened tray CMM measured distortion (b) Bending effect on battery tray (black arrows indicating the direction of pressing in coining operation).

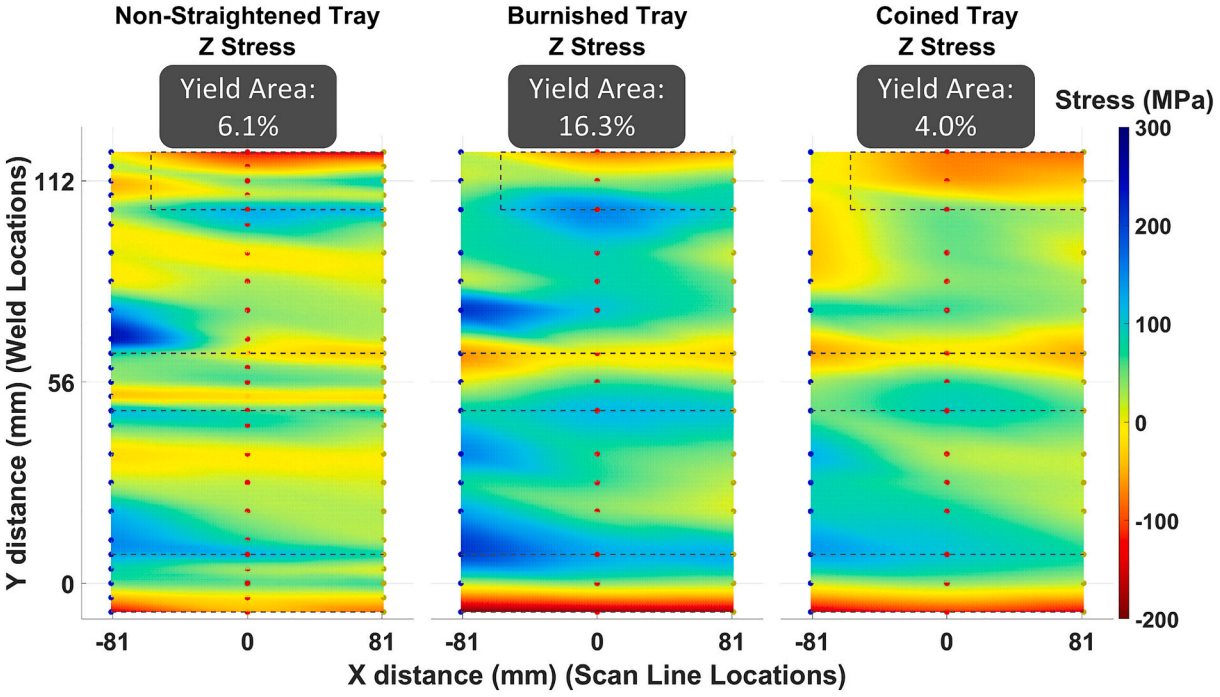

Fig. 20. Comparing (Z-direction) non-straightened to burnished and coined stress map.

(3) Following the burnishing operation, the measured residual stress in the scanned region revealed evidence of surface layer compression induced by the burnishing technique. In addition, the burnishing operation reduced the yield area by 14 and 18 % in the X-direction and Y-direction, respectively. In contrast, the Z-direction stresses increased the yield area by 10 % after the burnishing operation. Nonetheless, the burnishing operation restored 93 % of the battery tray's surface area to within ±0.75 mm of the pre-weld geometry.

(4) Following the coining operation, the yield area is reduced by 14 % in the X-direction of stresses. The yield area in the Z-direction stayed nearly constant, only decreasing by 2 %. However, the battery tray's significant distortion profile reduced by the operation required considerable plastic deformation to restore the pre-weld geometry, increasing the yield area by 23 % after straightening in the Y-direction of stress. Nevertheless, the coining operation restored 98 % of the battery tray's surface area to within ±0.75 mm of the pre-weld geometry.

This paper provides an improved understanding of the relationship between FSW parameters, straightening operations, and the corresponding alleviation or generation of residual stress. Subsequently, these results may be utilized to optimize the FSW process further, thereby minimizing the generation of residual stress in aluminum components, reducing component distortion, and ultimately leading to improved dimensional accuracy in the final product with lower production costs.

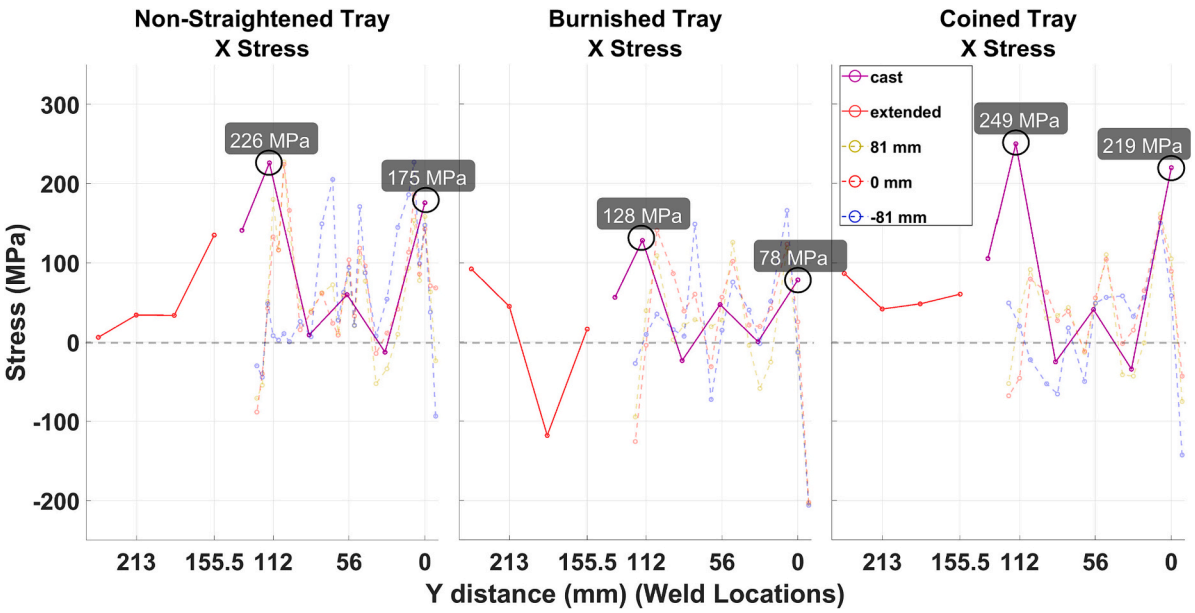

Fig. 21. All 5 Scan lines comparing straightening operations (X-direction).

Data availability

The raw data required to produce the residual stress results are available to download from Mendeley Data [https://doi.org/10.17632/dwm4vf8g3t.1].

Acknowledgments

This research was made possible in part due to the financial support of Nemak Canada. Additionally, a portion of this research used the expertise of Dr. Jeff Bunn and Paris Cornwell, which assisted with the experiment at the High Flux Isotope Reactor in the DOE Office of Science User Facility operated by the Oak Ridge National Laboratory.

References

[1] Khan NZ, Siddiquee AN, Khan ZA. Friction stir welding: dissimilar aluminum alloys. 1st ed. Boca Raton: CRC Press; 2017.
[2] Mohammadi J, Behnamian Y, Mostafaei A, Izadi H, Saeid T, Kokabi AH, et al. Friction stir welding joint of dissimilar materials between AZ31B magnesium and 6061 aluminum alloys: microstructure studies and mechanical characterizations. Mater Charact 2015;101:189–207. https://doi.org/10.1016/j.matchar.2015.01.008.
[3] Cole EG, Fehrenbacher A, Duffie NA, Zinn MR, Pfefferkorn FE, Ferrier NJ. Weld temperature effects during friction stir welding of dissimilar aluminum alloys 6061-t6 and 7075-t6. Int J Adv Manuf Technol 2014;71:643–52. https://doi.org/10.1007/s00170-013-5485-9.
[4] Threadgillll PL, Leonard AJ, Shercliff HR, Withers PJ. Friction stir welding of aluminium alloys. Int Mater Rev 2009;54:49–93. https://doi.org/10.1179/174328009X411136.
[5] El-Sayed MM, Shash AY, Abd-Rabou M, ElSherbiny MG. Welding and processing of metallic materials by using friction stir technique: a review. J Adv Join Process 2021;3:1–20. https://doi.org/10.1016/j.jajp.2021.100059.
[6] Richards DG, Prangnell PB, Williams SW, Withers PJ. Global mechanical tensioning for the management of residual stresses in welds. Mater Sci Eng A 2008;489:351–62. https://doi.org/10.1016/j.msea.2007.12.042.
[7] Delijaicov S, de Oliveira Silva PA, Resende HB, Batalha MHF. Effect of weld parameters on residual stress, hardness and microstructure of dissimilar AA2024-T3 and AA7475-T761 friction stir welded joints. Mater Res 2018;21:1–11. https://doi.org/10.1590/1980-5373-mr-2018-0108.
[8] Zhang T, He Y, Shao Q, Zhang H, Wu L. Comparative Study on fatigue properties of friction stir welding joint and lap joint. In: 13th Int. Conf. Fract. 2013, ICF 2013. 2; 2013. p. 1604–13.
[9] Richards DG, Prangnell PB, Withers PJ, Williams SW, Nagy T, Morgan S. Efficacy of active cooling for controlling residual stresses in friction stir welds. Sci Technol Weld Join 2010;15:156–65. https://doi.org/10.1179/136217109X12590746472490.
[10] de Giorgi M, Scialpi A, Panella FW, de Filippis LAC. Effect of shoulder geometry on residual stress and fatigue properties of AA6082 FSW joints. J Mech Sci Technol 2009;23:26–35. https://doi.org/10.1007/s12206-008-1006-4.
[11] He J, Ling Z, Li H. Effect of tool rotational speed on residual stress, microstructure, and tensile properties of friction stir welded 6061-T6 aluminum alloy thick plate. Int J Adv Manuf Technol 2016;84:1953–61. https://doi.org/10.1007/s00170-015-7859-7.
[12] Peel M, Steuwer A, Preuss M, Withers PJ. Microstructure, mechanical properties and residual stresses as a function of welding speed in aluminium AA5083 friction stir welds. Acta Mater 2003;51:4791–801. https://doi.org/10.1016/S1359-6454(03)00319-7.
[13] Nie L, Wu YX, Gong H. Prediction of temperature and residual stress distributions in friction stir welding of aluminum alloy. Int J Adv Manuf Technol 2020;106:3301–10. https://doi.org/10.1007/s00170-019-04826-4.
[14] Masubuchi K. Analysis and control of residual stresses, distortion and their consequences in welded structures. London: Pergamon; 1982.
[15] Feng Z. Processes and mechanisms of welding residual stress and distortion. Cambridge England: Woodhead; 2005.
[16] Leggatt RH. Residual stresses in welded structures. Int J Press Vessel Pip 2008;85:144–51. https://doi.org/10.1016/j.ijpvp.2007.10.004.
[17] Jayaraman N, Prevéy P, Mahoney M. Fatigue life improvement of an aluminum alloy FSW with low plasticity burnishing. In: TMS Annu. Meet.; 2003. p. 259–69.
[18] Altenkirch J, Steuwer A, Withers PJ, Williams SW, Poad M, Wen SW. Residual stress engineering in friction stir welds by roller tensioning. Sci Technol Weld Join 2009;14:185–92. https://doi.org/10.1179/136217108X388624.
[19] Woo W, Feng Z, Wang XL, Brown DW, Clausen B, An K, et al. In situ neutron diffraction measurements of temperature and stresses during friction stir welding of 6061-T6 aluminium alloy. Sci Technol Weld Join 2007;12:298–303. https://doi.org/10.1179/174329307X197548.
[20] Kumar N, Hussain M. Comparative study of FSW strength versus plate overlap. Int J Eng Res Technol 2019;8:645–9. www.ijert.org.
[21] Wang L, Makhlouf M, Apelian D. Aluminium die casting alloys: alloy composition, microstructure, and properties-performance relationships. Int Mater Rev 1995;40:221–38. https://doi.org/10.1179/imr.1995.40.6.221.
[22] Hidnert P, Krider HS. Thermal expansion of aluminum and some aluminum alloys. J Res Natl Bur Stand 1934;48(1952):209. https://doi.org/10.6028/jres.048.030.
[23] Sediako D, D'Elia F, Lombardi A, MacHin A, Ravi Ravindran C, Hubbard C, et al. Application of neutron diffraction in analysis of residual stress profiles in the cylinder web region of an as-cast v6 ai engine block with cast-in fe liners. In: SAE Tech. Pap. 2; 2011. p. 299–308.
[24] Liu T, Bunn JR, Fancher CM, Nastac L, Arvikar V, Levin I, et al. Neutron diffraction analysis of residual strain in high-pressure die cast A383 engine blocks. J Mater Eng Perform 2020;29:5428–34. https://doi.org/10.1007/s11665-020-05019-x.
[25] Sabry N, Stroh J, Sediako D. Characterization of microstructure and residual stress following the friction stir welding of dissimilar aluminum alloys. CIRP J Manuf Sci Technol 2023;41:365–79. https://doi.org/10.1016/j.cirpj.2022.11.021.
[26] ASTM E8. ASTM E8/E8M standard test methods for tension testing of metallic materials 1. Annu B ASTM Stand 2010;4:1–27. https://doi.org/10.1520/E0008.
[27] Pauleau Y. Materials surface processing by directed energy techniques. Elsevier Science; 2006.
[28] Lemmen HJK, Alderliesten RC, Pieters RRGM, Benedictus R, Pineault JA. Yield strength and residual stress measurements on friction-stir-welded aluminum alloys. J Aircr 2010;47:1570–83. https://doi.org/10.2514/1.C000212.

[29] Bhardwaj S, Ratnayake RMC. Challenges due to welds fabricated at a close proximity on offshore structures, pipelines, and piping: state of the art. In: Proc Int Conf Offshore Mech Arct Eng - OMAE. 3; 2020. p. 2016–8. https://doi.org/10.1115/OMAE2020-18586.

[30] Bhardwaj S, Chandima Ratnayake RM. Residual stress estimation in defect assessment procedures at weld toe and away locations on girth welds: review of key parameters. Theor Appl Fract Mech 2021;111:102848. https://doi.org/10.1016/j.tafmec.2020.102848.

[31] Sun Z, Wu CS. A numerical model of pin thread effect on material flow and heat generation in shear layer during friction stir welding. J Manuf Process 2018;36:10–21. https://doi.org/10.1016/j.jmapro.2018.09.021.

[32] Schmidt H, Hattel J, Wert J. An analytical model for the heat generation in friction stir welding, model. Simul Mater Sci Eng 2004;12:143–57. https://doi.org/10.1088/0965-0393/12/1/013.

[33] Bolognesi Donato GH, Magnabosco R. Modeling and characterization of residual stresses in material processing. Elsevier; 2014. https://doi.org/10.1016/B978-0-08-096532-1.00218-1.

[34] Kianfar S, Aghaie E, Stroh J, Sediako D, Tjong J. Residual stress, microstructure, and mechanical properties analysis of HPDC aluminum engine block with cast-in iron liners. Mater Today Commun 2021;26:101814. https://doi.org/10.1016/j.mtcomm.2020.101814.

[35] Jamshidi Aval H. Microstructure and residual stress distributions in friction stir welding of dissimilar aluminium alloys. Mater Des 2015;87:405–13. https://doi.org/10.1016/j.matdes.2015.08.050.